Excitation of the Madden–Julian Oscillation in Atmospheric Adjustment to Equatorial Heating

Yu Liang, Alexey V. Fedorov, Vladimir Zeitlin, Patrick Haertel

To cite this version:

Yu Liang, Alexey V. Fedorov, Vladimir Zeitlin, Patrick Haertel. Excitation of the Madden–Julian Oscillation in Atmospheric Adjustment to Equatorial Heating. Journal of the Atmospheric Sciences, 2021, 78 (12), pp.3933-3950. 10.1175/jas-d-21-0092.1 . hal-03646665

HAL Id: hal-03646665
https://hal.science/hal-03646665v1

Submitted on 23 Feb 2023

Excitation of the Madden–Julian Oscillation in Atmospheric Adjustment to Equatorial Heating

YU LIANG,[a] ALEXEY V. FEDOROV,[a,b] VLADIMIR ZEITLIN,[c] AND PATRICK HAERTEL[a]

[a] *Department of Earth and Planetary Sciences, Yale University, New Haven, Connecticut*
[b] *LOCEAN/IPSL, Sorbonne University, Paris, France*
[c] *Laboratoire de Météorologie Dynamique, Sorbonne University/Ecole Normale Supérieure/CNRS, Paris, France*

(Manuscript received 2 April 2021, in final form 7 September 2021)

ABSTRACT: We study the adjustment of the tropical atmosphere to localized surface heating using a Lagrangian atmospheric model (LAM) that simulates a realistic Madden–Julian oscillation (MJO)—the dominant, eastward-propagating mode of tropical intraseasonal variability modulating atmospheric convection. Idealized warm sea surface temperature (SST) anomalies of different aspect ratios and magnitudes are imposed in the equatorial Indian Ocean during MJO-neutral conditions and then maintained for 15 days. The experiments then continue for several more months. Throughout these experiments, we observe a robust generation of an MJO event, evident in precipitation, velocity, temperature, and moisture fields, which becomes a key element of atmospheric adjustment along with the expected Kelvin and Rossby waves. The MJO circulation pattern gradually builds up during the first week, and then starts to propagate eastward at a speed of 5–7 m s^{-1}. The upper-level quadrupole circulation characteristic of the MJO becomes evident around day 14, with two anticyclonic gyres generated by the Gill-type response to convective heating and two cyclonic gyres forced by the excited Kelvin waves and extratropical Rossby wave trains. A moisture budget analysis shows that the eastward propagation of the MJO is controlled largely by the anomalous advection of moisture and by the residual between anomalous moisture accumulation due to converging winds and precipitation. The initial MJO event is followed by successive secondary events, maintaining the MJO for several more cycles. Thus, this study highlights the fundamental role that the MJO can play in the adjustment of the moist equatorial atmosphere to localized surface heating.

KEYWORDS: Convection; Kelvin waves; Rossby waves; Madden-Julian oscillation; General circulation models

1. Introduction

Tropical heating, caused by latent heat release in deep convective clouds (Yanai et al. 1973), is an important driver of atmospheric general circulation in the tropics and beyond. Using linear shallow-water models on the equatorial beta plane, the classical papers of Matsuno (1966) and Gill (1980) and subsequent studies (e.g., Heckley and Gill 1984) demonstrated that as a resting atmosphere responds to a localized heating, a low-level easterly flow builds up to the east of the heating through the eastward propagation of equatorial Kelvin waves, while a westerly flow develops to the west of the heating due to westward-propagating Rossby waves. The generation of propagating Kelvin and Rossby waves is a fundamental feature of the equatorial atmospheric and oceanic adjustments (e.g., Fedorov and Brown 2009). Likewise, the steady-state response to a heating, or the so-called Gill response combining stationary Rossby and Kevin wave patterns, provides a primary framework for understanding tropical circulations such as the Walker and Hadley cells and the South Asian monsoon. Further studies using barotropic or multilevel baroclinic models find that in the presence of upper-level mean westerly flow, quasi-barotropic Rossby wave trains can also be generated in response to tropical heating. These Rossby wave trains propagate into middle and high latitudes (Hoskins and Karoly 1981; Webster 1981; Lau and Lim 1984; Jin and Hoskins 1995), giving rise to tropical–extratropical teleconnections such as the Pacific–North American (PNA) pattern (Wallace and Gutzler 1981).

Although the aforementioned and subsequent studies investigated many critical aspects of the atmospheric response to tropical heating, and the heating prescribed in the models represented latent heat release, most of those shallow-water studies used in effect ‘‘dry’’ models that did not have water vapor and moist convection. A question then arises of how the solution of the classical ‘‘dry’’ Matsuno–Gill problem would change in the presence of active moist convective dynamics. Addressing this question is one of the main goals of the present study.

Recently, within a two-layer shallow-water model of the tropical atmosphere which incorporates in a simple way the transport of moisture, its condensation, and latent heat release, it has been shown (Rostami and Zeitlin 2020) that the adjustment of localized large-scale pressure anomalies leads to the appearance of transient structures resembling to some degree the Madden–Julian oscillation (MJO), in addition to the long equatorial waves produced by the ‘‘dry’’ adjustment of the same anomalies (Le Sommer et al. 2004). Such response is absent in the ‘‘dry’’ Matsuno–Gill problem. While a conjecture was made by Rostami and Zeitlin (2020) that the MJO could be induced by the moist-convective equatorial adjustment, representing the MJO in ‘‘moist’’ shallow-water models remains a

---

Supplemental information related to this paper is available at the Journals Online website: https://doi.org/10.1175/JAS-D-21-0092.s1.

Corresponding author: Yu Liang, yu.liang@yale.edu

DOI: 10.1175/JAS-D-21-0092.1

big challenge. General circulation models (GCMs) have also failed so far to generate primary MJO events in response to imposed warm sea surface temperature (SST) anomalies and the corresponding convective heating of the atmosphere (e.g., Nakajima et al. 2004; Maloney and Sobel 2007). Accordingly, our objective is to investigate whether indeed the MJO can be generated as part of atmospheric adjustment to localized surface heating in a full-scale Lagrangian general circulation model (Haertel et al. 2014, 2017), which is known to realistically reproduce the MJO. Our choice of surface heating perturbations is motivated by observations as discussed later.

The MJO is the dominant mode of intraseasonal atmospheric variability in the Indo-Pacific (Madden and Julian 1972; Rui and Wang 1990; Wheeler and Kiladis 1999; Kiladis et al. 2005; Zhang 2005, 2013). Interactions between moist thermodynamics, convection, radiation, and large-scale circulation are believed to be vital for its mechanisms (Majda and Stechmann 2009, 2011; Sobel and Maloney 2012, 2013; Adames and Kim 2016; Sentić et al. 2020; Wang and Rui 1990; Haertel et al. 2014, 2017; Haertel 2018; Rostami and Zeitlin 2020; Khairoutdinov and Emanuel 2019; Zhang et al. 2020, and references therein).

Considering a similar cloud morphology between the MJO and convectively coupled Kelvin and Rossby waves (Kiladis et al. 2009; Mapes et al. 2006), and the potential role of Kelvin and Rossby waves in the MJO multiscale structure (Majda and Stechmann 2009, 2011), one could ask, If the model resolves moist convection, can the MJO be excited by tropical heating? In fact, during the Dynamics of the MJO (DYNAMO) field campaign (Yoneyama et al. 2013), for about 2 weeks before the initiation of one of the detected MJO events, the equatorial Indian Ocean experienced anomalous SST warming (Fig. 1) up to 3°C (Moum et al. 2014), suggesting a potential role of warm SST anomalies in generating the MJO. Previous studies have also shown that introducing temporal and/or spatial variability in SST boundary conditions can increase MJO activity (e.g., Pegion and Kirtman 2008; Stan 2018; Kim et al. 2008). In particular, Stan (2018) examined the MJO response to adding or removing SST variability at time scales ranging from diurnal to 5-day to intraseasonal to interannual.

The MJO is characterized by an eastward-propagating, planetary-scale envelope of clouds and precipitation modulating the wind field (e.g., Madden and Julian 1972; Zhang 2005). MJO events usually originate in the Indian Ocean, mature over the Maritime Continent, and dissipate soon after crossing the date line in the Pacific (Rui and Wang 1990), although some events may emerge over the Maritime Continent or decay before reaching the western Pacific (Matthews 2008; Zhang and Ling 2017). The slow eastward-propagation speed ($\sim 5\,\mathrm{m\,s^{-1}}$), planetary scales, and distinct upper-level quadrupole circulation distinguish the MJO from convectively coupled equatorial waves (Kiladis et al. 2005, 2009). The MJO affects a number of global climate and weather phenomena (see a review by Zhang 2013), including the onset and demise of Asian and Australian monsoons (Hendon and Liebmann 1990; Lau and Chan 1986), extreme rainfall and temperature anomalies (Jones et al. 2004; Chang et al. 2005), tropical cyclogenesis (Liebmann et al. 1994; Liang and Fedorov 2021), and El Niño–Southern Oscillation (McPhaden 1999; Kessler and Kleeman 2000; Liang et al. 2021).

Due to its oscillatory nature and global impacts, the MJO serves as a source of predictability for medium-range weather forecasts (Zhang 2013). However, GCMs still struggle to properly simulate the MJO, and even state-of-the-art models do not necessarily capture the full amplitude, vertical structure, and eastward propagation of the MJO (Hung et al. 2013; Jiang et al. 2015). The prediction skill of the MJO remains limited in climate and weather forecasting models (Janiga et al. 2018; Kim et al. 2019), especially for the primary (initial) MJO events that are not preceded by an active MJO (Matthews 2008). This calls for a better understanding of the MJO physics, including its initiation mechanisms.

Here, using the Lagrangian atmospheric model (LAM) that realistically simulates the MJO, for the first time to our knowledge we show that in addition to Kelvin and Rossby waves, the excitation of the MJO is indeed an essential component of the moist atmospheric adjustment to equatorial heating, which has important implications for the mechanisms of MJO generation and for MJO prediction. Our numerical experiments and analysis, including a column-integrated moisture budget analysis, clearly illustrate the physical processes involved in the initiation and evolution of the primary MJO event, complementing observational and other modeling studies which are usually based on composites of multiple MJO events (e.g., Rui and Wang 1990; Kiladis et al. 2005; Adames and Kim 2016; Adames and Wallace 2015). Finally, in line with previous studies (e.g., Kiladis et al. 2005; Sobel and Maloney 2013; Adames and Kim 2016), we show that the upper-level quadrupole circulation, a salient feature of the MJO, is closely related to the equatorial Rossby and Kelvin waves and extratropical Rossby wave trains excited by convective heating associated with the MJO.

2. Numerical model and methods

a. Lagrangian atmospheric model

The numerical model used for the current study is the LAM, which simulates a robust and realistic MJO (Fig. 2; also see Haertel et al. 2014, 2017). The LAM represents atmospheric circulation by tracking a collection of conforming air parcels whose horizontal motions are predicted by Newtonian mechanics:

$$\frac{d\mathbf{x}}{dt} = \mathbf{v}, \tag{1}$$

$$\frac{d\mathbf{v}}{dt} + f\mathbf{k} \times \mathbf{v} = \mathbf{A}_p + \mathbf{A}_m, \tag{2}$$

where $\mathbf{x}$ is the horizontal location, t is time, $\mathbf{v}$ is the horizontal velocity, f is the Coriolis parameter, $\mathbf{k}$ is the vertical unit vector, $\mathbf{A}_p$ is the horizontal acceleration of the parcel caused by pressure, and $\mathbf{A}_m$ is the horizontal acceleration from parameterized turbulent mixing of momentum. Nonconvective vertical motions are implicitly determined by mass continuity.

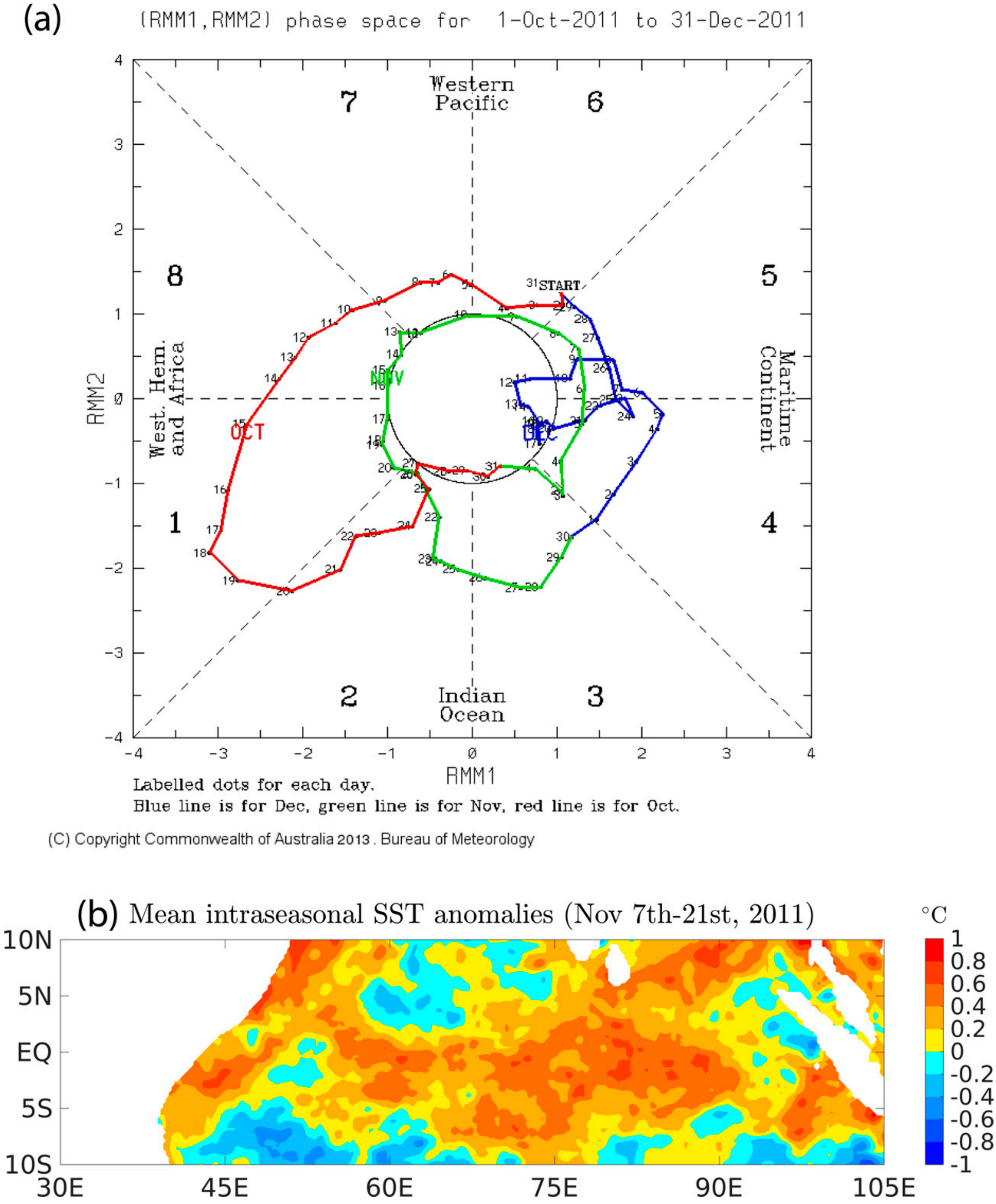

FIG. 1. (a) The MJO phase-space diagram for 1 Oct to 31 Dec 2011 during the DYNAMO experiment. RMM1 and RMM2 are indices based on the outgoing longwave radiation (OLR) and zonal winds at upper and lower levels of the atmosphere, which indicate the location and amplitude of the MJO event (Wheeler and Hendon 2004). When the phase-space trajectory of the system defined by the two indices stays within the black circle, the MJO is considered to be in the neutral phase; otherwise, the MJO is in the active phase. Note that in our study we actually use a slightly different definition of the MJO phase based on the standard deviation of precipitation anomalies (section 2). The diagram is from http://www.bom.gov.au/climate/mjo/. (b) Intraseasonal SST anomalies in the equatorial Indian Ocean averaged between 7 and 21 Nov 2011, when the MJO was close to the neutral phase [see the green line along the black circle in (a)]. The second MJO observed in the DYNAMO experiment initiated in the Indian Ocean on 21 Nov 2011, according to the phase-space diagram. Intraseasonal SST anomalies are calculated relative to the 90-day running-mean value. The SST data are from NOAA Optimum Interpolation SST v2 product (www.esrl.noaa.gov/psd/data).

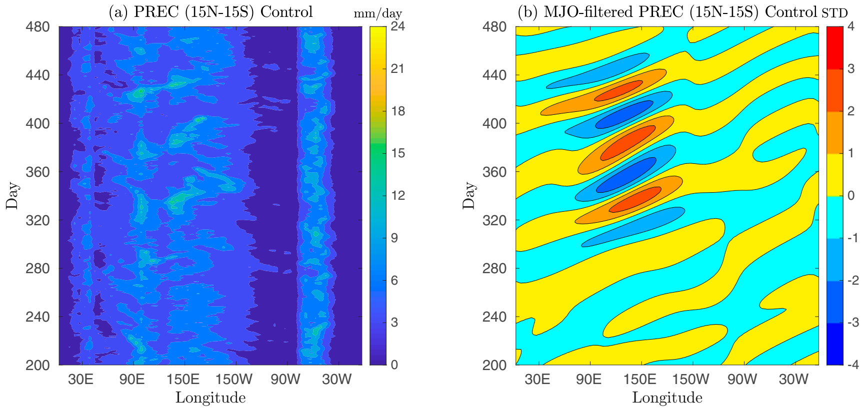

FIG. 2. Hovmöller diagrams for (a) raw precipitation and (b) MJO-filtered precipitation along the equator (colors) averaged between 15°N and 15°S for the Control experiment (day 200 to day 480). The space–time filtering is used to retain the eastward-propagating MJO signals with zonal wavenumbers 1–5 and periods of 30–95 days (Wheeler and Kiladis 1999). The standard deviation of the filtered rainfall between 60°E and 180° is 0.88 mm day^{-1}. Note that 20 ensemble members are used for the perturbation experiments. They are initiated using atmospheric conditions of the Control experiment on days 260 to 269.5, when the MJO is in the neutral phase.

The LAM and its oceanic counterpart, the Lagrangian ocean model (LOM), have been developed over the past decade and have been successfully applied to a variety of weather, climate, and ocean phenomena (Haertel and Fedorov 2012; Haertel et al. 2014, 2017; Haertel 2018, 2019).

The LAM is a global atmospheric GCM with a realistic land configuration and topography (Haertel et al. 2017). It utilizes a Lagrangian overturning representation of convection: convection is triggered (i.e., parcels exchange vertical positions) if an air parcel is warmer than the surrounding parcels. By rearranging the vertical positions of Lagrangian parcels and mixing them with the environment in convective regions, the model captures the observed net effects of vertical transports and mixing by convective plumes, as measured by mean profiles of temperature and moisture, as well as the mean patterns of tropical precipitation and convective organization (Haertel et al. 2014). The entrainment/mixing parameter in the model has been tuned to simulate a realistic MJO and atmospheric mean vertical temperature profiles.

The Lagrangian approach has advantages over Eulerian methods for the simulation of the MJO because 1) it captures the observed sensitivity of convective divergence profiles to atmospheric moisture and stratification, which is an important factor for the MJO to build up moisture on its leading edge (Haertel et al. 2008); 2) the moisture transport in the Lagrangian model can be calculated without numerical diffusion, maintaining the tight moisture gradient in the MJO, which is important for modeling the eastward moisture transport by the low-level equatorial westerly wind anomalies associated with the MJO; and 3) the LAM reproduces a fairly realistic mean state (Haertel et al. 2017), especially the background westerly winds in the western equatorial Pacific and the mean precipitation field (Fig. 2), which may be important for the MJO simulation (Kim et al. 2011).

The LAM configuration in this study has an equivalent Eulerian horizontal resolution of approximately 1° on the equator; the radius of the parcels (in kilometers) does not change with latitude. The robust simulation of the MJO at this relatively coarse horizontal resolution is another advantage of the LAM. The vertical resolution of the model is approximately 31 hPa and the time step of integration is 15 min with the output saved every 6 h. Last, the land surface temperature in the LAM is computed using a simple land surface model, with a single layer of ground whose water-holding capacity is 25 mm. The land surface model has a heat capacity equivalent to that of 0.1 m of water and uses observed albedo values (Haertel et al. 2017).

For the convenience of analysis, we postprocess the model output by averaging the dynamical and precipitation fields on 6° longitude × 6° latitude Eulerian grids, and for dynamical fields, they are further averaged vertically at an interval of 50 hPa. This relatively coarse resolution helps to filter out small-scale spatial variability while retaining large-scale features. Most of the analysis in the paper is based on this 6° Eulerian grid data.

b. *Experimental setup*

One Control and three main perturbation experiments have been conducted. The Control experiment is forced by the observed March climatological SST averaged for years 1990–2010; insolation is fixed for 15 March with a diurnal cycle. The Control experiment is integrated for 2 years to obtain a sufficient number of MJO events. March is chosen because it is when the MJO is the most symmetric about the equator and active in the LAM.

For the perturbation experiments we impose idealized SST perturbations with a Gaussian shape centered at the equator at 75°E and computed as follows:

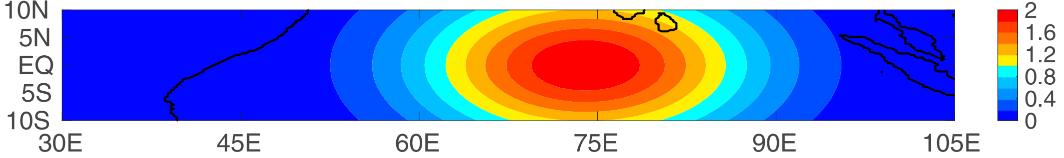
(a) SST perturbation 2°C-Aspect1

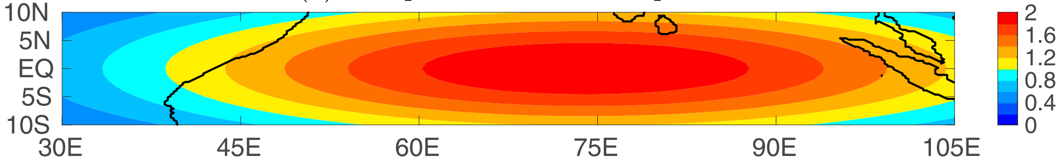
(b) SST perturbation 2°C-Aspect3

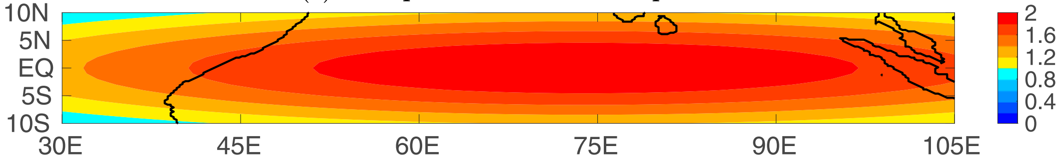
(c) SST perturbation 2°C-Aspect5

FIG. 3. The SST perturbations (colors, °C) used in the (a) Aspect 1, (b) Aspect3, and (c) Aspect5 experiments with a 2°C maximum amplitude.

$$\mathrm{SST_{pert}} = \mathrm{Amp_{SST}}\ \exp[-(\mathrm{longitude} - 75°\mathrm{E})^2/2/(r \times 10°)^2]\ \exp(-\mathrm{latitude}^2/2/10°^2)$$
$$\text{for} \quad r = 1, 3, 5. \tag{3}$$

The meridional decay scale of the Gaussian function is set to 10° of latitude. In the main suite of experiments the amplitude of the SST perturbation $\mathrm{Amp_{SST}}$ is set to 2°C but the aspect ratio r is varied ($r = 1, 3, 5$). Perturbation experiments with different aspect ratios of the imposed SST perturbation are referred to as Aspect1, Aspect3, and Aspect5 (Fig. 3). In addition, to explore the sensitivity of the results, we conduct two other sets of perturbation experiments wherein we set the magnitude of the SST perturbation to 1° and 5°C. Such warm SST perturbations are similar to the persistent SST anomaly observed in the Indian Ocean during the DYNAMO campaign (Fig. 1).

c. Ensemble approach

Like conventional GCMs, the LAM generates synoptic variability that may affect MJO generation. To reduce the effect of this variability on the results, we apply an ensemble approach using a 20-member ensemble for each perturbation experiment. New ensemble members are obtained by shifting the imposed temperature perturbation progressively by 12 h, i.e., the SST perturbation is added starting on day 260, 260.5, . . . , 269.5 of the Control experiment. For all these slightly different initial conditions, the MJO remains in the neutral phase (see Fig. 2b; the MJO neutral phase is defined below). The SST perturbation is maintained for 15 days, after which the climatological March SST is used to force the experiments. All perturbation experiments are integrated until day 350. After integration, for the analysis presented in Figs. 4–10, we shift the time origin for each ensemble member, defining day 0 as the first day when the SST perturbation is applied.

Because ensemble experiments have different initial conditions, each generates distinct synoptic variability, leading to slight differences in the MJO evolution, which allows us to achieve statistically significant results by averaging between different ensemble members. The results presented in the next sections are based on such ensemble averages.

As we are generally interested in large-scale features of the atmospheric response to tropical convective heating, the ensemble-mean anomalous fields are further smoothed by applying 1–2–1 filters five times zonally and three times meridionally. The significance level of anomalies between the perturbation experiments and the Control experiment is calculated using the two-sample Student's t test whose sample sizes are 20.

d. Bandpass space–time filtering of the MJO signal

A bandpass filter (retaining zonal wavenumbers 1–5 and periods of 30–95 days) is applied when necessary to isolate the eastward-propagating MJO signals (Wheeler and Kiladis 1999). An example of filtered precipitation along the equator averaged between 15°N and 15°S in the Control experiment is shown in Fig. 2b where three consecutive MJO events can be seen.

Using the model precipitation field, we define the convective phase of the MJO when the MJO-filtered precipitation anomalies averaged between 15°N and 15°S are positive and exceed one standard deviation of the Control experiment in the region between 60°E and 180°, where the MJO rainfall is most pronounced. Similarly, the suppressed phase of the MJO is defined when MJO-filtered precipitation anomalies, again averaged between 15°N and 15°S, are negative and their magnitude exceeds one standard deviation. Otherwise, the MJO is said to be in the neutral phase. The standard deviation of filtered precipitation in this region of the Control experiment is 0.88 mm day^{-1}. We can further calculate the MJO propagation speed by estimating the slope of the precipitation-weighted

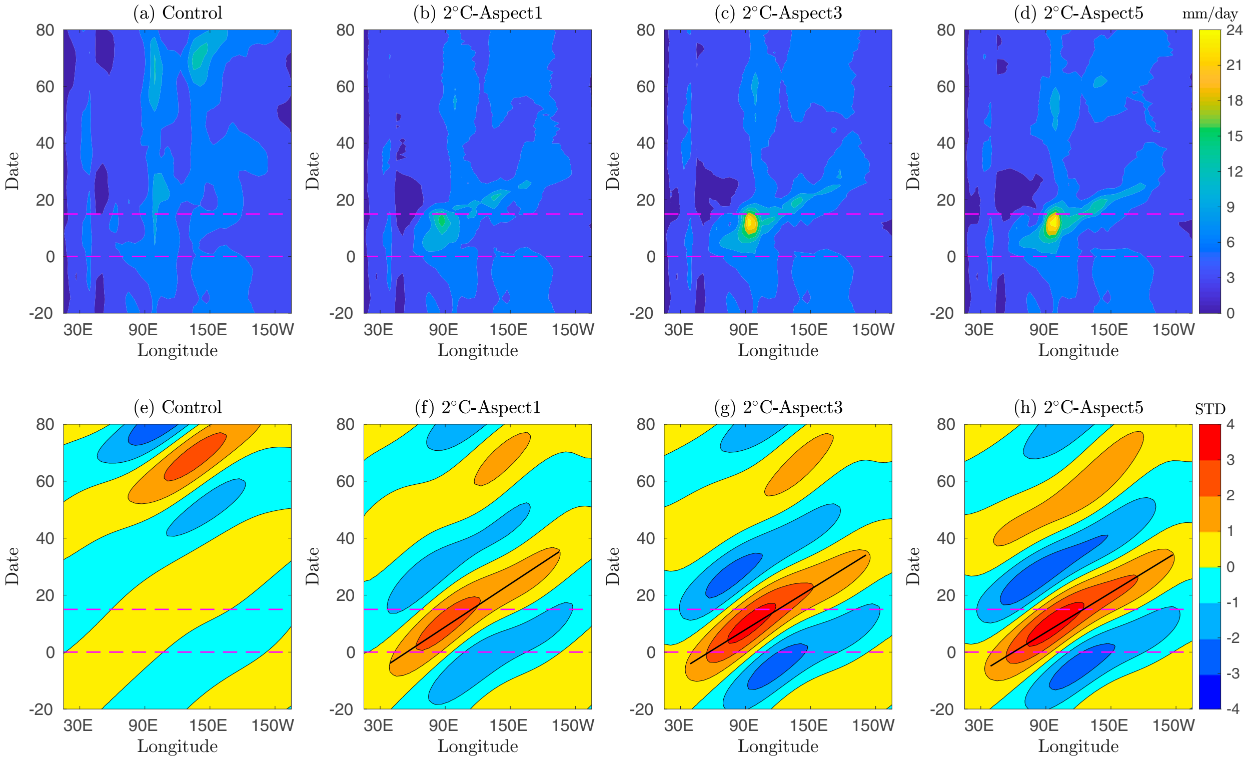

FIG. 4. Hovmöller diagrams of ensemble-mean precipitation (colors, mm day^{-1}) along the equator averaged between 15°N and 15°S for the (a) Control and for (b) Aspect1, (c) Aspect3, and (d) Aspect5 experiments. The maximum amplitude of the imposed SST anomaly is 2°C. (e)–(h) The same precipitation field but with a bandpass space–time filter applied to isolate the eastward-propagating MJO signal with zonal wavenumbers 1–5 and periods of 30–95 days (following Wheeler and Kiladis 1999). The Aspect5 experiment corresponds to the SST perturbation with the largest zonal scale. Date 0 corresponds to when the SST perturbation is first added. The dashed magenta lines indicate the 15-day interval when the SST perturbation is applied. In (e)–(h), positive values beyond one standard deviation of the filtered precipitation calculated for 60°E–180° (~0.9 mm day^{-1}) indicate the convective phase of the MJO; negative values indicate the suppressed phase. The inclined black lines indicate the precipitation-weighted linear least squares fit for the convective MJO path. Here and in the subsequent figures, ensemble-mean results averaged over 20 ensemble members are shown, and dates are relative to the time when the SST perturbation is first added.

linear least squares fit for the convective MJO path on a Hovmöller diagram. The amplitude of the MJO is defined as the maximum filtered precipitation averaged in the region of 15°S–15°N, 90°–150°E.

e. *Moisture budget analysis*

Next, we use a moisture budget analysis to diagnose mechanisms of the MJO eastward propagation in the perturbation experiments. The column-integrated moisture tendency in the perturbation and Control experiments can be calculated as follows:

$$\langle \partial_t q \rangle = -\langle q \nabla \cdot \mathbf{u} \rangle - \langle \mathbf{u} \nabla q \rangle + E - P, \tag{4}$$

where q is specific humidity, $\mathbf{u}$ is horizontal velocity, E is evaporation, P is precipitation, ∇ indicates the horizontal gradient operator (a vector), and $\nabla \cdot$ indicates the horizontal divergence. Here, $\langle x \rangle$ is a mass-weighted column integral of variable x between the model top and surface pressure levels:

$$\langle x \rangle = \int_{p_{\mathrm{top}}}^{p_{\mathrm{surface}}} x\, dp/(g\rho_w), \tag{5}$$

where ρ_w is the density of water, p is pressure, and g is the acceleration of gravity.

Let $C = -\langle q \nabla \cdot \mathbf{u} \rangle$ and $A = -\langle \mathbf{u} \nabla q \rangle$, which are the accumulation of moisture due to converging winds and the advection of moisture, respectively. We can rewrite Eq. (4) as

$$\langle \partial_t q \rangle = C + A + E - P. \tag{6}$$

Calculating the anomalous moisture tendency in the perturbation experiments relative to the Control experiment yields

$$\langle \partial_t q' \rangle = C' + A' + E' - P', \tag{7}$$

where primes indicate anomalies relative to the Control experiment. Later we will use the anomalous precipitation and moisture fields to isolate and describe the excited MJO in the perturbation experiments. Note that the terms in Eq. (7) are first calculated for each ensemble member of the perturbation experiments relative to the Control experiment, in reference to the date when the SST perturbation is first added; they are then averaged among the ensemble members and smoothed applying a simple 1–2–1 average to obtain the ensemble-mean results (as discussed in section 2c).

One can further decompose C' and A' given that $\mathbf{u} = \mathbf{u}_{\mathrm{contr}} + \mathbf{u}'$ and $q = q_{\mathrm{contr}} + q'$, and get

$$C' = -\langle q_{\mathrm{contr}} \nabla \cdot \mathbf{u}' \rangle - \langle q' \nabla \cdot \mathbf{u}_{\mathrm{contr}} \rangle - \langle q' \nabla \cdot \mathbf{u}' \rangle , \qquad (8)$$

$$A' = -\langle \mathbf{u}' \nabla q_{\mathrm{contr}} \rangle - \langle \mathbf{u}_{\mathrm{contr}} \nabla q' \rangle - \langle \mathbf{u}' \nabla q' \rangle , \qquad (9)$$

where the subscript *contr* indicates variables in the Control experiment. Here, the $-\langle q_{\mathrm{contr}} \nabla \cdot \mathbf{u}' \rangle$ term, for example, represents the contribution from the accumulation of the control moisture due to anomalous converging winds. Finally, the column-integrated anomalous moisture tendency can also be calculated explicitly from the temporal evolution of the anomalous moisture field.

3. Results

a. The excitation of the MJO

As the system responds to the imposed 2°C SST perturbation, a clear convective MJO-like signal develops in the composites of the precipitation field during the first 30 days of the perturbation experiments (Figs. 4b–d). The excited MJO originates in the central equatorial Indian Ocean, propagates eastward and decays near the date line. It is not preceded by active MJO events but is followed by successive MJO events absent in the Control experiment. A bandpass space–time filtering, retaining the eastward-propagating intraseasonal signals (Figs. 4f–h), further highlights the MJO excitation (note that the weak MJO signals between days −20 and 0 is an artifact of the filtering).

Among the three perturbation experiments with different aspect ratios of the imposed SST perturbation, the amplitude of the excited MJO is the largest in the Aspect5 experiment, and the eastward-propagation speed is also the fastest ($\sim$5.5 m s^{-1}). That the newly generated primary MJO event is followed by another one is especially clear in the Aspect5 experiment (Figs. 4d,h), even though the bandpass filter artificially smooths the MJO spatial features. This secondary event, although not as strong as the primary one, develops on around day 40. Similar results are seen in the 1°C and 5°C experiments (Figs. S1 and S2 in the online supplement), confirming that the excitation of the MJO is an essential component of the moist atmospheric adjustment to localized tropical heating regardless of the magnitude or aspect ratio of the SST perturbation. The newly generated MJO event, followed by the succeeding events, alters the entire MJO evolution with implications for the MJO prediction.

b. The evolution and dynamical structures of the excited MJO

To take a closer look at the excited MJO, we examine several snapshots of the composite precipitation, winds and the corresponding streamfunction for the 2°C-Aspect3 perturbation experiment (Fig. 5); anomalous fields are used to describe the excited MJO, and hereafter no bandpass filtering is used unless noted. We note that some of these anomalous fields may have contributions both from the excited MJO and from the stationary response to the heating due to the imposed SST perturbation. However, as we shall see in Figs. 5 and 6, most of this anomalous precipitation propagates eastward in a coherent manner. The propagation continues even when the SST anomaly is switched off. These factors suggest the dominant role of the excited MJO event in generating the aforesaid anomalies. On day 6, a basinwide positive precipitation anomaly has already developed in the equatorial Indian Ocean. It is centered around 75°E (near the middle of the SST perturbation), suggesting the newly generated MJO is gradually developing in the first week yet without much eastward propagation. In the meantime, a relatively weak dry signal is observed in the western equatorial Pacific, similar to the pattern observed in previous studies (Rui and Wang 1990; Wheeler and Hendon 2004). The anomalous winds in the lower troposphere (850 hPa) exhibit the classical Gill-type response (Fig. S3a), while the wind reversal at the upper level (200 hPa) (Fig. 5a) indicates the first baroclinic structure in the vertical. Two well-defined Rossby gyres, centered around 15°–20°N/S, develop to the north and south of the positive precipitation anomaly.

By day 10, both positive and negative precipitation anomalies have propagated eastward with slightly strengthened signals. The two Rossby gyres have also intensified in terms of their sizes and wind speeds (Fig. 5b). The MJO upper-level quadrupole circulation starts to form at this time but is still not well defined. Compared to the MJO precipitation anomalies, the upper-level westerly (Kelvin) front travels significantly faster (also see Fig. 6). On day 10, it has already reached the west coast of South America while the MJO precipitation center is still in the eastern equatorial Indian Ocean.

On day 14, when the MJO precipitation center reaches the Maritime Continent, the positive precipitation anomaly has its maximum amplitude, and the dry precipitation signal over the western-central equatorial Pacific disappears. In the meantime, a new dry region starts to form in the southwestern Indian Ocean (Fig. 5c). The Kelvin wave front by this time has almost traveled across the entire circumference of the globe and started to interact with the easterly winds of the Rossby wave front. The two Rossby gyres to the west of the positive precipitation anomaly continue to strengthen and expand poleward. Most importantly, two cyclonic gyres to the east of the positive precipitation anomaly are now clearly observed, composing the MJO upper-level quadrupole circulation. This quadrupole circulation has a global scale (zonal wavenumber 1) and resembles the observed horizontal structure of the MJO (Kiladis et al. 2005). In the lower troposphere, the two cyclonic Rossby gyres (Fig. S3c) are more confined to the tropics, and no anticyclonic gyre circulation is observed to the east of the positive precipitation center, which is also consistent with the observations (Kiladis et al. 2005).

On day 18, the positive precipitation anomaly continues to propagate eastward but after reaching the western Pacific starts to weaken. Dry regions in the equatorial Indian Ocean and over east Africa expand, similar to the observations (Rui and Wang 1990). The upper-level quadrupole circulation is still evident, but off-equatorial positive precipitation anomalies start to detach from the positive precipitation center. On day

(a) Day 6 composite perturbation 200hPa wind, stream function and precipitation fields

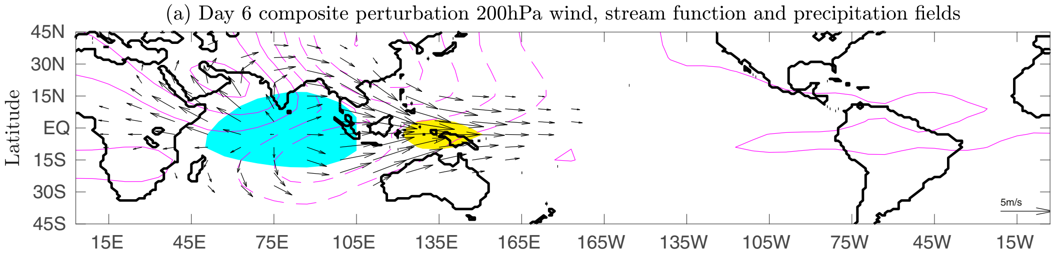

(b) Day 10 composite perturbation 200hPa wind, stream function and precipitation fields

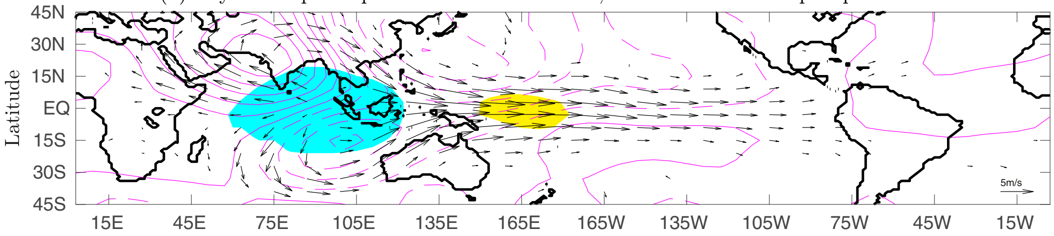

(c) Day 14 composite perturbation 200hPa wind, stream function and precipitation fields

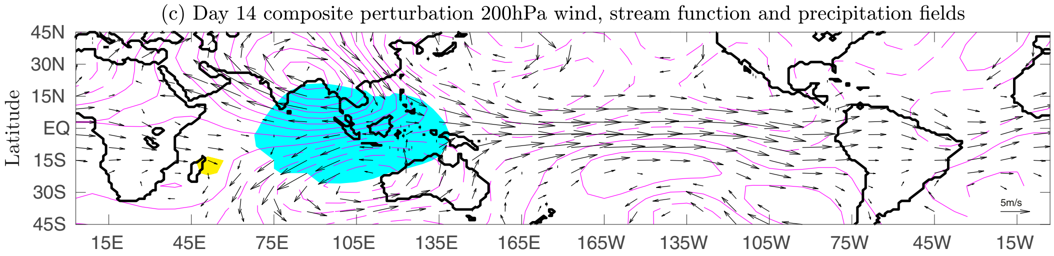

(d) Day 18 composite perturbation 200hPa wind, stream function and precipitation fields

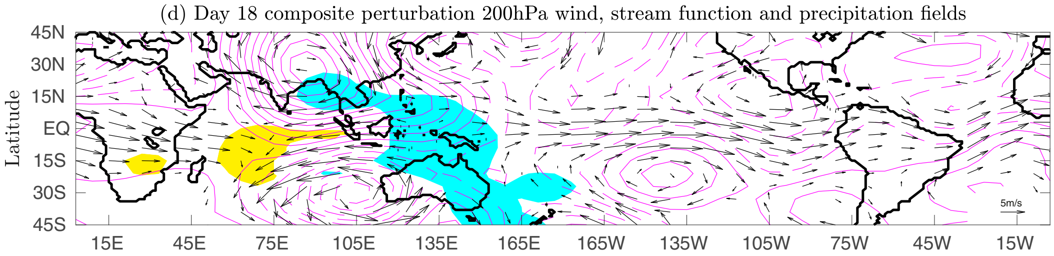

(e) Day 22 composite perturbation 200hPa wind, stream function and precipitation fields

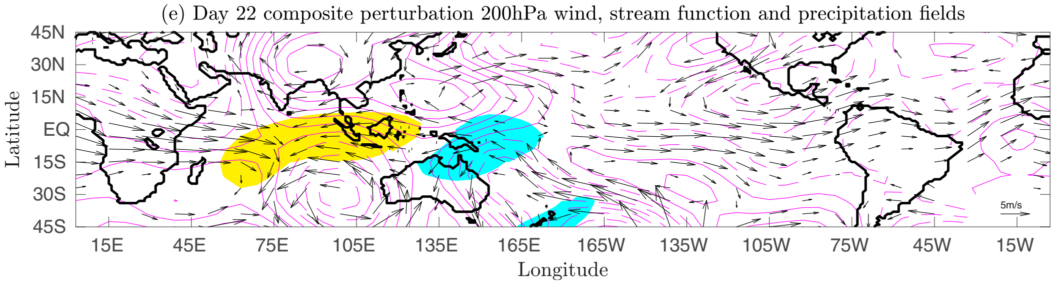

FIG. 5. Longitude–latitude snapshots of anomalous winds at 200 hPa and the corresponding anomalous streamfunction and anomalous precipitation fields on days (top to bottom) 6, 10, 14, 18, and 22 in the Aspect3 experiment using the 2°C SST perturbation. The anomalous fields are smoothed using 1–2–1 filters (section 2c). Anomalous wind vectors are shown as black arrows, based on which the streamfunction (magenta contours) is calculated. Note the zonal average of the streamfunction is removed to highlight the MJO structure. The contour interval is $2 \times 10^6\ \mathrm{m^2\,s^{-1}}$, with solid and dashed contour lines starting at 1×10^6 and $-1 \times 10^6\ \mathrm{m^2\,s^{-1}}$, respectively. Cyan and yellow shading indicates anomalous precipitation exceeding 1.5 and $-1.5\ \mathrm{mm\,day^{-1}}$, respectively. Only statistically significant wind vectors and precipitation at the 95% level are shown. The significance level is calculated using the two-sample Student's *t* test. Note the eastward propagation of positive precipitation anomalies and the quadrupole structure of the MJO flow (especially pronounced after day 10).

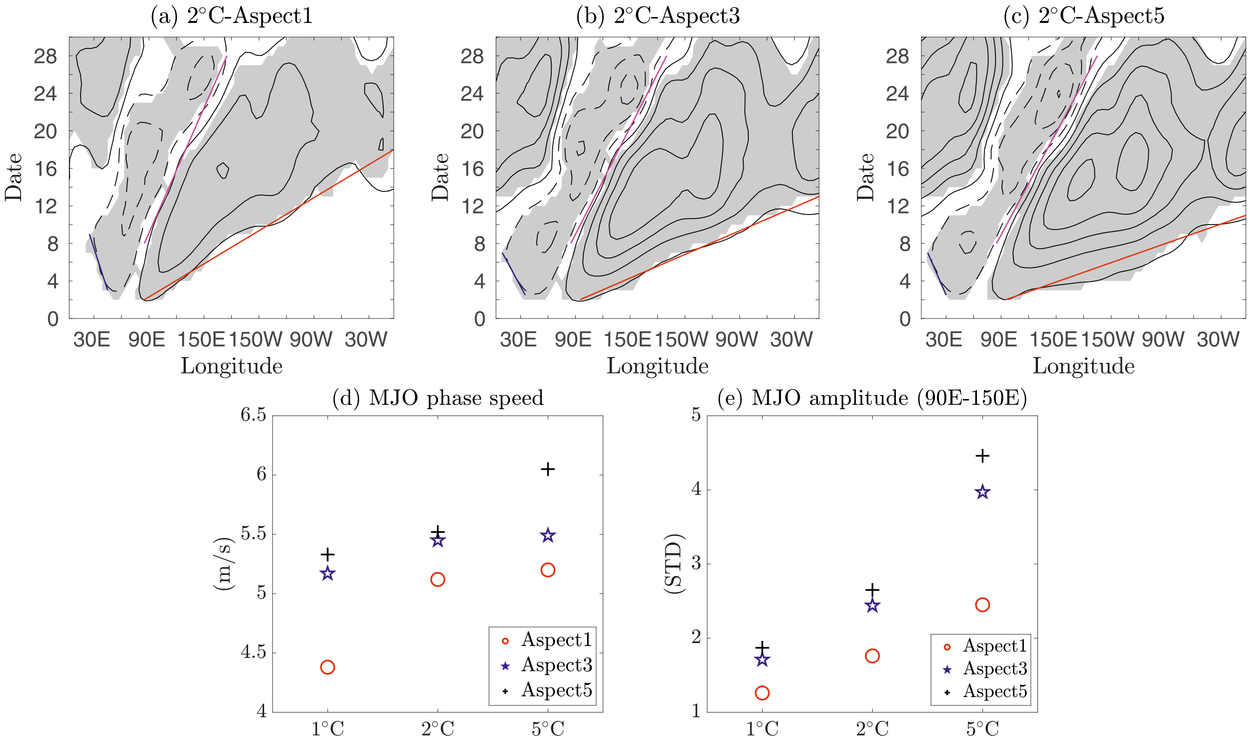

FIG. 6. Hovmöller diagrams of anomalous zonal winds at 200 hPa as a function of time and longitude along 3°N for the (a) Aspect1, (b) Aspect3, and (c) Aspect5 experiments with a 2°C SST perturbation magnitude. The contour interval is 2 m s^{-1} with solid and dashed contour lines starting at 1 and -1 m s^{-1}, respectively. Gray shading indicates values that are locally statistically significant at the 95% level. Blue, red, and magenta lines indicate the propagation of the Rossby wave front, the Kelvin wave front, and the MJO, respectively. (d) The phase speed and (e) the amplitude of the MJO in the 1°, 2°, and 5°C perturbation experiments for different aspect ratios of the SST perturbation. The speed of the MJO is estimated from the slope of the precipitation-weighted linear least squares fit for the convective MJO path (see Figs. 4f–h). The amplitude of the MJO is defined as the maximum filtered precipitation averaged for the region 15°S–15°N, 90°–150°E. One standard deviation is around 0.9 mm day^{-1}.

22, the two western Rossby gyres detach from the positive equatorial precipitation anomaly, and two new Rossby gyres start to form, maintaining the MJO quadrupole circulation. This emanation of Rossby waves has been used to explain the mechanisms of the boreal summer intraseasonal oscillation (Wang and Xie 1997). After day 22, large-scale synoptic variability generated at midlatitudes appears to dominate the anomalous flow; thereafter perturbation fields are not shown.

The propagation of Rossby and Kelvin waves, and the MJO, can be easily inferred from Hovmöller diagrams showing upper-level winds for example at 3°N (Fig. 6 and Figs. S4, S5). The westward propagation (about 5° longitude day^{-1}, or 6 m s^{-1}) of the Rossby wave front and the eastward propagation (about 23° longitude day^{-1}, or 30 m s^{-1}) of the Kelvin wave front, indicated by the blue and red lines, respectively, in Fig. 6b, are clearly observed. The two fronts establish westerly and easterly wind anomalies, respectively, in the upper troposphere. The speeds of the two fronts are significantly lower than the reported speeds in similar experiments with a dry model, which were about 10° longitude day^{-1} and 34° longitude day^{-1}, respectively (Jin and Hoskins 1995). The coupling between circulation and moist convection slows down the speed of fronts' propagation, making it closer to the speed of convectively coupled equatorial Rossby and Kelvin waves (Kiladis et al. 2009).

The MJO, as indicated by the magenta line between solid and dashed contours (Fig. 6b), propagates eastward at a speed of 5–6 m s^{-1} from the equatorial Indian Ocean to the central Pacific. It accelerates a little when reaching the western Pacific, possibly due to the detachment of the two Rossby gyres. This acceleration is also reported in previous observational studies (Jiang et al. 2015). Note that both the MJO event and the Kelvin wave front have larger amplitudes and travel faster when stronger SST perturbations are imposed (Fig. 6), which is indicative of nonlinear effects on the wave dynamics. Nonlinear Kelvin wave fronts are known to travel faster than the linear ones, and the nonlinear correction to the speed is proportional to the wave amplitude (Fedorov and Melville 2000).

The vertical structure of the atmospheric adjustment is examined in Fig. 7 where longitude–height cross sections of composite perturbation zonal wind, temperature and specific humidity along the equator averaged between 9°N and 9°S are shown for the 2°C-Aspect3 experiment on day 6 and 14. The first baroclinic structure of the planetary-scale zonal wind anomalies is evident in Figs. 7a and 7b, with the node located around 400 hPa, in agreement with the modal structure of the observed MJO (Adames and Kim 2016; Haertel 2021). In response to the imposed heating, the entire equatorial troposphere experiences warming with a maximum temperature

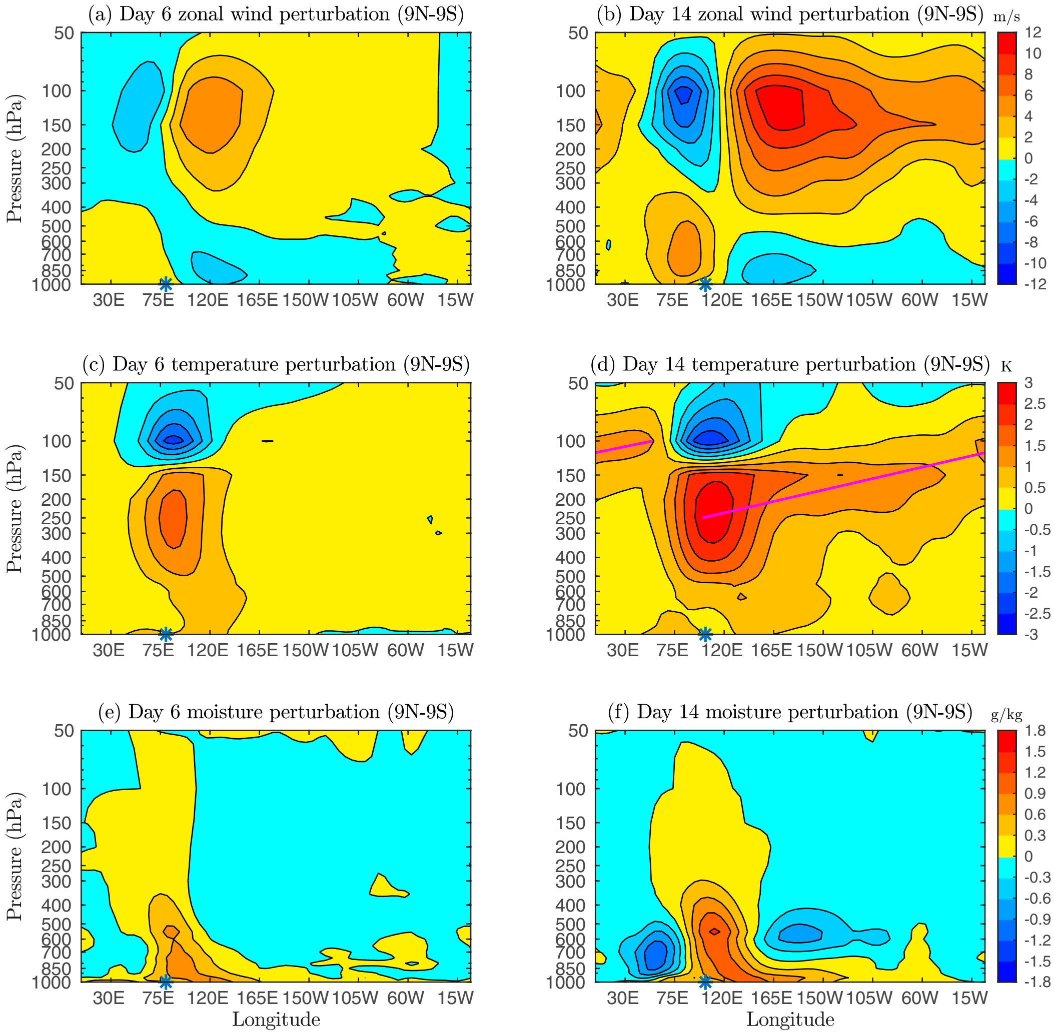

FIG. 7. Snapshots of the longitude–height cross section of anomalies in (a),(b) zonal wind, (c),(d) temperature, and (e),(f) specific humidity along the equator averaged between 9°N and 9°S on (left) day 6 and (right) day 14 for the Aspect3 experiment with a 2°C SST perturbation magnitude. The days are relative to the date when the SST perturbation is first added. The solid magenta line in (d) indicates the eastward and upward propagation of Kelvin waves. Blue stars indicate the center of positive rainfall anomalies, which is calculated by the weighted average of positive rainfall anomalies between 9°N and 9°S.

increase around 250 hPa, above which a strong cooling signal develops (Figs. 7c,d). This cooling signal may be caused in part by the adiabatic lifting of air above deep convection (Sherwood et al. 2003). To the east of the positive precipitation anomaly center there exists a region of warming in the lower and middle troposphere, spanning nearly 100° of longitude, which is particularly clear in Figs. S6c and S6d. This effect has been attributed to shallow and congestus convection in the observed MJO, which destabilizes the atmospheric column and favors the eastward propagation of the MJO (Kiladis et al. 2005). In Fig. 7d, the eastward and upward propagation of Kelvin waves indicated by the magenta solid line is especially clear. Marked by the maximum temperature perturbation, the temperature signal of the MJO also slowly propagates eastward. Note a low-level warm anomaly centered above 75°E—it does not propagate and is directly related to the imposed SST perturbation.

The planetary scale and eastward propagation of the MJO are also clear in the anomalous moisture field, where the midlevel moisture anomaly collocates with the upper-level warm temperature anomaly, providing the moisture source for precipitation (Bretherton et al. 2004). A long equatorial band (up to 150° of longitude in Fig. 7f) of positive anomalous moisture in the boundary layer, above which the air is dry, extends to the east of the MJO precipitation, similar to the observations (Kiladis et al. 2005). This can be caused by enhanced evaporation due to anomalous surface easterlies (Sperber 2003) associated with the excited MJO and in part by the direct effect of the warm SST perturbation on the boundary layer, given that prevailing winds in the central-eastern tropical Pacific are easterly. Shallow convection ahead of the MJO can also contribute to the moistening of the boundary layer, and we will discuss the anomalous moisture field in more detail later in section 3c. A strong dry signal is also observed at the trailing edge of the MJO precipitation, consistent with the reduced precipitation in Fig. 5c.

Note that the magnitude of temperature anomalies associated with the excited MJO event is several times stronger than the observed composites of MJO anomalies (e.g., Kiladis et al. 2005). In part, this is because by construction observational composite analyses average events that have different structures, magnitudes, and locations, thus diluting the signal, while here we focus on one strong primary MJO event. Other factors include 1) the SST perturbation itself exerts a mean heating effect on the troposphere and 2) the calculated perturbation field includes other intraseasonal signals, especially the strong Kelvin waves. In Fig. S6, where the bandpass filtering is used to isolate the MJO signal, the magnitude and structure of the composite MJO-filtered perturbation fields are generally comparable to the observations.

c. Mechanisms for the eastward propagation of the excited MJO

Moisture buildup to the east of the MJO convective center is essential for the MJO's eastward propagation (Maloney 2009; Majda and Stechmann 2009, 2011; Andersen and Kuang 2012; Sobel and Maloney 2013; Sobel et al. 2014; Adames and Wallace 2015; Kim et al. 2019). To investigate mechanisms of the eastward propagation of the excited MJO in the perturbation experiments, we conduct a column-integrated anomalous moisture budget analysis for the 2°C-Aspect3 experiment on day 10, when the MJO convective anomaly is still in the eastern equatorial Indian Ocean but is about to cross into the Maritime Continent. The terms of the moisture budget averaged between 30°N and 30°S are shown in Fig. 8a [cf. Eq. (7)].

Anomalous accumulation of moisture due to converging winds (C') is found to be positively correlated with rainfall anomalies, with the two terms almost canceling each other. Nevertheless, as the anomalous moisture accumulation leads rainfall anomalies by a few degrees of longitude (Fig. 8a), their residual, referred to as a "column process" in several studies (e.g., Chikira 2014; Wolding and Maloney 2015), is nearly in quadrature with positive rainfall anomalies (Fig. 8b). Centered on the equator, the residual moistens the atmosphere to the east of the positive rainfall anomalies and dries the atmosphere to the west, contributing to the eastward propagation of the excited MJO, in agreement with the previous analysis based on observational and reanalysis data (Adames and Wallace 2015). As the column-integrated anomalous moisture is only about 10% of the background moisture field, C' is dominated by the $-\langle q_{\mathrm{contr}} \nabla \cdot \mathbf{u}' \rangle$ term: the anomalous accumulation of the control moisture due to converging anomalous winds [cf. Eq. (8)]. Examining the vertical structure of C' further reveals that its leading component is mostly confined below 850 hPa (Fig. S7), pointing to the importance of the atmospheric boundary layer for the eastward propagation of the MJO.

The anomalous advection of moisture averaged over the tropical band (A') also moistens the air to the east of the positive rainfall anomalies and dries to the west (Figs. 8a,c), which therefore strongly contributes to the eastward propagation of the excited MJO. The moistening to the east and poleward of the positive rainfall anomalies is especially prominent in the Southern Hemisphere, which can explain the enhanced precipitation over Australia later on day 18 (cf. Fig. 5d).

In addition, we have conducted moisture budget analyses for the Control and perturbation experiments, respectively, in Fig. S8 [see Eq. (6)]. They show that the advection term dries the tropical atmospheric column in both experiments, but in the perturbation experiments the drying effect is weaker to the east of the positive precipitation anomalies and stronger to the west. This may be related to suppressed eddy activity to the east of the precipitation anomalies due to the Kelvin wave response and enhanced eddy activity to the west due to the Rossby wave response (e.g., Andersen and Kuang 2012; Sobel and Maloney 2013).

Returning to the analysis in Fig. 8, we observe that the anomalous evaporation term, centered around 75°E and mainly forced by the warm SST perturbation and westerly wind anomalies, has some contribution to the moisture buildup to the east. However, as it is mostly located to the west of the positive precipitation anomalies, it would retard the eastward propagation of the excited MJO event. We find that the evaporation term is only important during the first week when it contributes strongly to the growth of the MJO amplitude. The sum of the four key terms shown in Fig. 8a is in quadrature with the positive rainfall anomalies and agrees with the explicitly calculated moisture tendency term relatively well, while the difference between the two should be mainly due to the horizontal and vertical averaging of data (section 2a) and the relatively low sampling rate (i.e., 6-hourly data).

Notice the strong zonal asymmetry of the anomalous moisture advection in Fig. 8c: the drying of the atmosphere to the west is centered on the equator while the moistening to the east is off the equator and much weaker. To understand the cause of this asymmetry, we further decompose the anomalous horizontal moisture advection into three terms following Eq. (9) (Fig. 9a), as was done in Jiang (2017) and references therein. Among the three terms, the advection of background (control) moisture by the anomalous flow ($-\langle \mathbf{u}' \nabla q_{\mathrm{contr}} \rangle$) and the advection of anomalous moisture by the anomalous flow ($-\langle \mathbf{u}' \nabla q' \rangle$) are the most important. As there is a strong meridional gradient in column-integrated moisture in the tropics, in the lower troposphere the anomalous equatorward flow of the Rossby gyres to the west of the positive rainfall anomalies causes drying on the poleward and western flanks of the positive rainfall anomalies while the poleward flow to the east causes moistening on the poleward and eastern flanks (Fig. 9b). The horizontal structure of the $-\langle \mathbf{u}' \nabla q_{\mathrm{contr}} \rangle$ term is generally symmetric about the positive rainfall center, exhibiting the quadrupole structure. The $-\langle \mathbf{u}' \nabla q' \rangle$ term on the other hand is mostly located to the west of the positive rainfall anomalies and centered at the equator (Fig. 9c), which is the main cause of the zonal asymmetry of the anomalous moisture advection. This is mainly because the zonal gradient of anomalous moisture to the west of the positive rainfall anomalies is much tighter than that to the east, therefore the drying effect is also stronger to the west.

As the anomalous accumulation of moisture due to converging winds has a strong contribution from the Kelvin wave component, while the anomalous moisture advection is dominated by the Rossby wave component, these results indicate

(a) Column intergrated anomalous moisture budget for 30N-30S for day 10

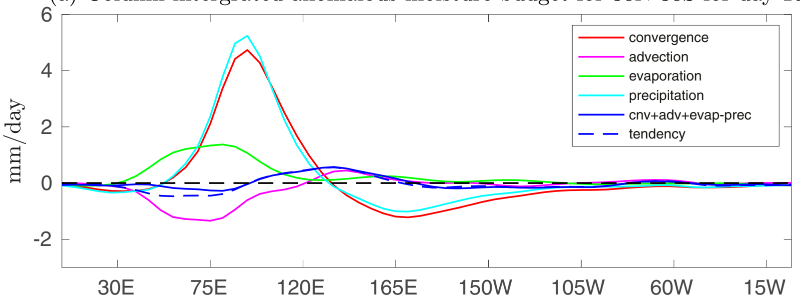

(b) Anomalous convergence minus anomalous precipitation

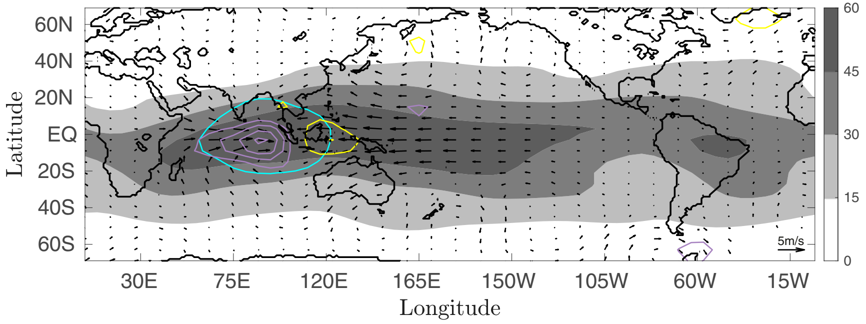

(c) Anomalous horizontal moisture advection

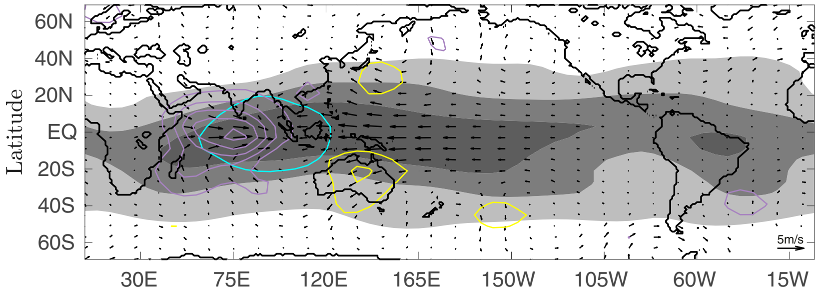

FIG. 8. (a) Key terms of the column-integrated anomalous moisture budget of the generated primary MJO event averaged between 30°N and 30°S on day 10 for the 2°C-Aspect3 perturbation experiment [Eq. (7)]. The convergence term (red line) represents the anomalous moisture accumulation due to converging winds (C'); the advection term (magenta line) represents the anomalous advection of moisture (A'). (b) The horizontal structure of the residual of column-integrated anomalous moisture accumulation due to converging winds minus anomalous precipitation. (c) The horizontal structure of anomalous column-integrated moisture advection. Yellow contours indicate moistening of the atmosphere with a contour interval of 0.5 mm day^{-1} starting at 0.5 mm day^{-1}; purple contours indicate otherwise. The cyan contour indicates the positive precipitation anomaly exceeding 1.5 mm day^{-1}. Wind arrows indicate lower-level wind anomalies relative to the Control experiment averaged between 600 and 1000 hPa. Gray shading indicates the background column-integrated specific humidity (in mm) on day 10 from the Control experiment.

that the Kelvin and Rossby components of the MJO both contribute to the MJO eastward propagation.

We note that the anomalous winds in the lower troposphere can be driven not only by the MJO convective heating but also to some extent by the zonal pressure gradient associated with the stationary SST perturbation itself (e.g., Lindzen and Nigam 1987). Therefore, one should use caution when interpreting each term and comparing these results with previous MJO budget analyses where anomalous fields were attributed solely to the MJO (e.g., Andersen and Kuang 2012; Adames and Wallace 2015; Kim et al. 2019). Nevertheless, similar analyses as in Fig. 8 conducted for days 14 and 18 (Figs. S9, S10) have reached the same conclusions, which suggests that the imposed SST perturbation has only limited direct effect on the moisture budget.

Previous studies have also analyzed the moist static energy (MSE) budget to diagnose mechanisms of the MJO eastward propagation (e.g., Andersen and Kuang 2012; Maloney 2009),

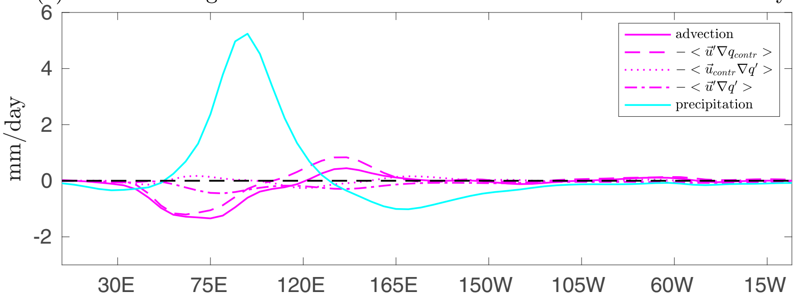
(a) Column intergrated anomalous moisture advection for 30N-30S for day 10

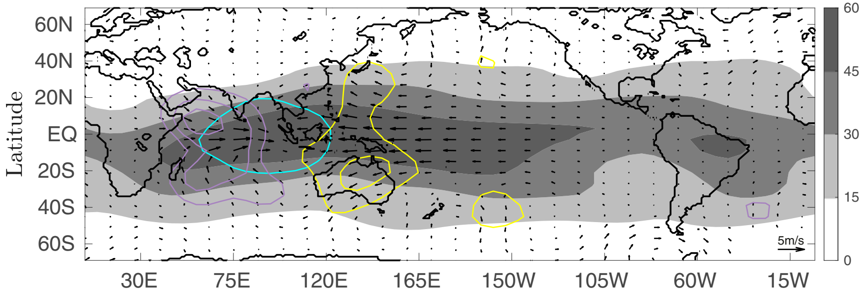
(b) Advection of Control moisture by the anomalous flow

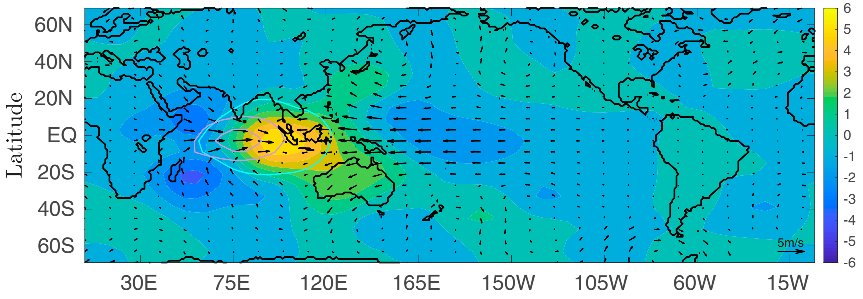
(c) Advection of anomalous moisture by the anomalous flow

FIG. 9. (a) As in Fig. 8a, but showing the anomalous horizontal moisture advection term A' and its three components [see Eq. (9)]. The horizontal structures of (b) the advection of background (Control) moisture by the anomalous flow and (c) the advection of anomalous moisture by the anomalous flow are shown in yellow and purple contours as in Figs. 8b and 8c. The color shading in (c) is the column-integrated anomalous moisture in the perturbation experiments relative to the Control experiment.

which allowed highlighting the role of longwave radiation. Here we analyze moisture budget rather than MSE budget because we identify the MJO using the precipitation field, which is directly related to the column-integrated moisture. An MSE budget analysis is planned for a follow-up paper.

d. Linkage between extratropical Rossby wave trains and the MJO quadruple circulation

An important salient feature of the MJO—the upper-level quadruple circulation—distinguishes the MJO from convectively coupled intraseasonal oscillations like Kelvin and Rossby waves. Here we explore the causes of this circulation in the excited primary MJO event. It has been noted that the quadruple circulation can develop in response to stationary heating and is associated with the extratropical Rossby wave trains (Jin and Hoskins 1995; Monteiro et al. 2014; Hu and Fedorov 2019). Indeed, on day 14 when the MJO quadruple circulation is apparent, two extratropical Rossby wave trains, one in each hemisphere, are seen to emanate from two anticyclonic Rossby gyres to the west of the positive precipitation anomalies as indicated by the meridional wind anomalies at 200 hPa (Fig. 10a). The wave trains have a zonal wavenumber of around 6 and, while propagating eastward, seem to be reflected equatorward by the poleward flank of the subtropical jets, in agreement with previous studies (Hoskins and Karoly 1981; Jin and Hoskins 1995). The equatorward flank of the extratropical Rossby waves (easterlies) and equatorial Kelvin waves (westerlies) act in tandem to form the two MJO cyclonic gyres above the Pacific in both hemispheres (cf. Fig. 5c).

(a) Day 14 composite perturbation meridional wind (200hPa)

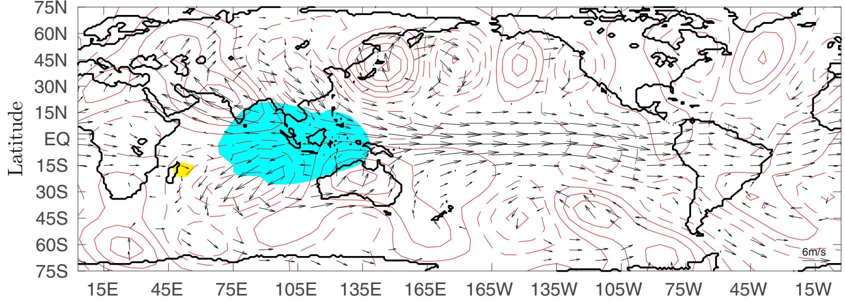

(b) Day 14 composite perturbation meridional wind (33N)

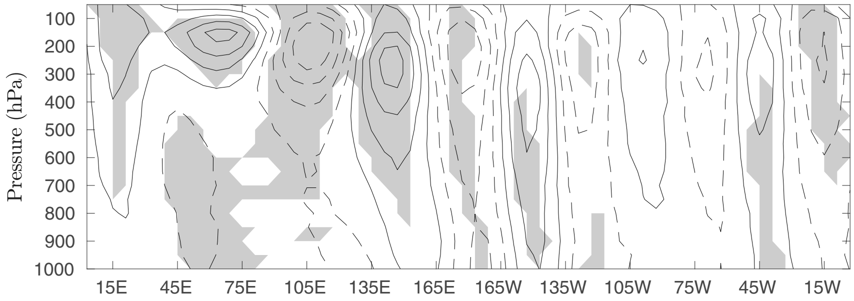

(c) Day 14 composite perturbation mean tropospheric temperature (200-850hPa)

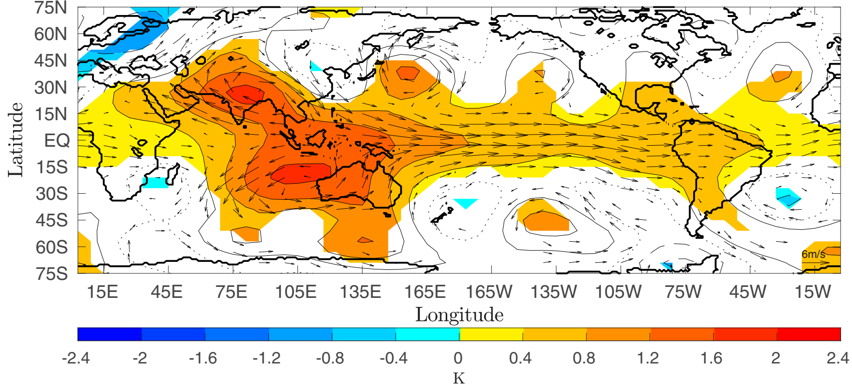

FIG. 10. (a) The longitude–latitude snapshot of composite meridional wind speed anomalies at 200 hPa (red contours) on day 14 for the 2°C-Aspect3 experiment. The contour interval is $1\ \mathrm{m\,s^{-1}}$ with solid and dashed contour lines starting at 0.5 and $-0.5\ \mathrm{m\,s^{-1}}$, respectively. Anomalous full wind vectors at 200 hPa are also shown (black arrows). In addition, cyan and yellow shadings indicate anomalous precipitation exceeding 1.5 and $-1.5\ \mathrm{mm\,day^{-1}}$, respectively. Only locally statistically significant wind vectors and precipitation at the 95% level are shown. (b) Anomalous meridional wind speeds as a function of pressure and longitude at 33°N (black contours) on the same day. The contour interval is $1\ \mathrm{m\,s^{-1}}$ with solid and dashed contour lines starting at 0.5 and $-0.5\ \mathrm{m\,s^{-1}}$, respectively. Gray shading marks the wind speed anomalies that are locally statistically significant at the 95% level. (c) The longitude–latitude snapshot of anomalous tropospheric temperature averaged between 200 and 850 hPa (contours and colors), which is an indication of the perturbation geopotential height at the 200-hPa level. The contour interval is 0.4 K with solid and dashed contour lines starting at 0.4 and -0.4 K, respectively. Dotted black contours indicate zero lines. Color shading indicates temperature anomalies (in K) that are locally statistically significant at the 95% level.

Note that the zonal wavenumber here (close to 6) is somewhat greater than that generated by observed MJO events (e.g., Mori and Watanabe 2008; Adames and Wallace 2014). This may be due to the fact that the subtropical jet has a slower speed and is displaced slightly more poleward in the LAM compared to observations.

A longitude–pressure cross section of anomalous meridional winds at 33°N shows the vertical structure of the Rossby wave train in the Northern Hemisphere (Fig. 10b). For the Rossby gyre to the west of positive precipitation anomalies, the first baroclinic feature is clear between 45° and 120°E. To the east of 135°E, however, the Rossby wave train is seen to be mostly quasi barotropic: the meridional wind perturbation is of the same sign across the entire troposphere. The quasi-barotropic Rossby wave train structure lasts for about three weeks before being deformed by baroclinic eddies in the midlatitudes. It appears that anticyclonic anomalies (relative to the Control experiment) dominate the atmospheric circulation within the Rossby wave trains (composed mostly of easterly wind anomalies at 30°N/S). This feature is also evident in the anomalous tropospheric temperature averaged between 200 and 850 hPa (Fig. 10c), which is indicative of geopotential height anomalies at 200 hPa. Like the initial warm Rossby gyres to the west of the positive precipitation anomalies, the excited Rossby wave trains are also dominated by the warm (high pressure) anticyclonic gyres, which leads to the prevalent easterlies in the subtropical Pacific (around 30°N/S) to the east of the positive precipitation anomalies. Similar results are also observed in the 1° and 5°C experiments.

4. Summary and discussion

Motivated by the observed anomalously warm sea surface temperature preceding the development of an MJO event detected during the DYNAMO campaign (Moum et al. 2014), we investigate the role of the MJO in the atmospheric adjustment to localized tropical surface heating, using an atmospheric GCM that simulates a realistic MJO. In a suite of experiments wherein we impose idealized SST anomalies in the equatorial Indian Ocean, in addition to the excitation of Kelvin and Rossby waves in response to the heating, a robust MJO event is generated as indicated by precipitation, zonal wind, temperature, and moisture fields. The primary MJO event is followed by consecutive, albeit weaker events. These results demonstrate that the MJO can indeed be an essential component of the equatorial atmospheric adjustment to localized heating, which has important implications for MJO modeling and prediction. Our results also indicate that in the presence of active moist convective dynamics the classical Matsuno–Gill problem, when describing transient atmospheric adjustment, should be modified to include MJO generation in addition to equatorial Kelvin and Rossby waves.

The amplitude of the excited MJO in the perturbation experiments ranges from 1 to 4 times the average MJO amplitude in the Control experiment, and the eastward-propagation speed varies from 4.4 to 6.3 $\mathrm{m\,s^{-1}}$ (Figs. 6d,e), depending on the size and magnitude of the imposed SST perturbation. In general, a stronger SST perturbation excites a stronger MJO propagating at a faster speed. The corresponding Kelvin waves also propagate faster, which may be dynamically related (Chen and Wang 2020).

Whereas many observational studies use composites of multiple MJO events including both primary and successive ones, in this study we are able to focus on primary MJO events (not preceded by other active MJO events) and hence analyze the primary MJO excitation. At first, in response to the imposed SST perturbation, a basinwide precipitation anomaly develops in the Indian Ocean as the troposphere is being convectively heated. During the first week, as atmospheric circulation and precipitation adjust to this heating, the generated MJO-like convective anomalies do not propagate eastward; negative precipitation (dry) anomalies develop in the western equatorial Pacific due to a lower-level divergence. Then the MJO starts to propagate eastward, reaching the speed of about 5.5 $\mathrm{m\,s^{-1}}$, and continues propagating even after the SST perturbation is turned off on day 15. The MJO amplitude peaks when the convective anomalies reach the Maritime Continent and gradually decays over the western Pacific, in agreement with previous observational studies (Rui and Wang 1990; Wheeler and Hendon 2004). Convection in the Indian Ocean weakens by day 20 (Figs. 5d,e), which may be related to the 40-day periodicity of the excited MJO in the model.

The mechanisms of the eastward propagation of the excited MJO events are investigated using a column-integrated anomalous moisture budget analysis. The anomalous accumulation of moisture due to converging winds and the anomalous advection of moisture are found to play the major role, similar to the analysis of Adames and Wallace (2015) and Andersen and Kuang (2012), the latter of which is based on the moist static energy budget. The anomalous accumulation of moisture due to converging winds is found to largely balance positive rainfall anomalies, but the residual, especially in the boundary layer, leads the MJO positive rainfall anomaly by a quarter phase, which favors the eastward propagation. Note that using the mass continuity equation and column integrated variables (e.g., Raymond et al. 2009), one can show that the anomalous accumulation of moisture due to converging winds is equivalent to the anomalous vertical advection of moisture, whose adiabatic component has been suggested to be important for convective growth in the MJO (Adames et al. 2021).

Additionally, the anomalous horizontal moisture advection moistens the eastern poleward flanks of the positive rainfall anomalies and dries the western poleward flanks. The meridional advection of the background moisture by the anomalous flow dominates the anomalous horizontal moisture advection, which is mainly forced by the cyclonic Rossby gyres in the lower troposphere. As the anomalous accumulation of moisture due to converging winds has a strong contribution from the Kelvin waves, these results indicate that the Kelvin and Rossby components of the MJO both contribute to the eastward propagation of the MJO.

We have also investigated the origin of the upper-level quadrupole circulation of the excited MJO. The two anticyclonic gyres to the west of the MJO precipitation, usually referred to as the Rossby gyres, develop as a direct Rossby wave response to the convective heating. The two cyclonic gyres to the east, however, appear to be formed mainly by the Kelvin waves (westerlies) and the equatorward flanks of extratropical Rossby wave trains (easterlies) emanating from the two anticyclonic Rossby gyres (Fig. 10c). This result contrasts previous composite studies suggesting that the two cyclonic gyres to the east of the MJO precipitation are caused by the equatorial Rossby wave response (Adames and Wallace 2014). However, this could be because their MJO composites consist of both primary and subsequent MJO events, and the latter are preceded by negative heating anomalies forcing cyclonic equatorial Rossby gyres. We also note that there is some negative tropospheric temperature signal in the MJO cyclonic gyre in the Southern Hemisphere, which may directly contribute to the formation of this cyclonic gyre. This negative temperature signal has been suggested to originate from the Rossby wave train trapped by the subtropical jet (cf. Fig. 2c of Monteiro et al. 2014), whose effect should be minor in this study.

Ultimately, our results highlight the important role of the MJO in the moist atmospheric adjustment to localized equatorial heating, with implications for the predictability of MJO events. Previous studies suggested that primary MJO events could be thermodynamically triggered by preceding dry conditions with a midtropospheric temperature anomaly destabilizing the atmosphere in the absence of coherent SST signals (Matthews 2008). In our study we show that an anomalous surface warming in the equatorial Indian Ocean can also act as a precursor of a primary MJO event, providing an important mechanism for MJO generation. The anomalous warming might arise from the ocean–atmosphere thermodynamic coupling during the dry period (Wang and Xie 1998) or can be caused by other factors. Accordingly, surface warming should be monitored closely for MJO prediction. Finally, further studies are needed to compare atmospheric response to equatorial heating across other models.

Acknowledgments. A.V.F. is supported by grants from NOAA (NA20OAR4310377) and NASA (NNX17AH21G), and the ARCHANGE project of the ''Make our planet great again'' program (CNRS, France). V.Z. is partially supported by the French National Program LEFE-IDAO. P.H. is supported by NSF Grant AGS-1561066.

Data availability statement. The model output data are being archived in https://doi.org/10.5061/dryad.x3ffbg7hz.

REFERENCES

Adames, Á. F., and J. M. Wallace, 2014: Three-dimensional structure and evolution of the MJO and its relation to the mean flow. *J. Atmos. Sci.*, **71**, 2007–2026, https://doi.org/10.1175/JAS-D-13-0254.1.

——, and ——, 2015: Three-dimensional structure and evolution of the moisture field in the MJO. *J. Atmos. Sci.*, **72**, 3733–3754, https://doi.org/10.1175/JAS-D-15-0003.1.

——, and D. Kim, 2016: The MJO as a dispersive, convectively coupled moisture wave: Theory and observations. *J. Atmos. Sci.*, **73**, 913–941, https://doi.org/10.1175/JAS-D-15-0170.1.

——, S. W. Powell, F. Ahmed, V. C. Mayta, and J. D. Neelin, 2021: Tropical precipitation evolution in a buoyancy-budget framework. *J. Atmos. Sci.*, **78**, 509–528, https://doi.org/10.1175/JAS-D-20-0074.1.

Andersen, J. A., and Z. Kuang, 2012: Moist static energy budget of MJO-like disturbances in the atmosphere of a zonally symmetric aquaplanet. *J. Climate*, **25**, 2782–2804, https://doi.org/10.1175/JCLI-D-11-00168.1.

Bretherton, C. S., M. E. Peters, and L. E. Back, 2004: Relationships between water vapor path and precipitation over the tropical oceans. *J. Climate*, **17**, 1517–1528, https://doi.org/10.1175/1520-0442(2004)017<1517:RBWVPA>2.0.CO;2.

Chang, C., P. A. Harr, and H.-J. Chen, 2005: Synoptic disturbances over the equatorial South China Sea and western Maritime Continent during boreal winter. *Mon. Wea. Rev.*, **133**, 489–503, https://doi.org/10.1175/MWR-2868.1.

Chen, G., and B. Wang, 2020: Circulation factors determining the propagation speed of the Madden–Julian oscillation. *J. Climate*, **33**, 3367–3380, https://doi.org/10.1175/JCLI-D-19-0661.1.

Chikira, M., 2014: Eastward-propagating intraseasonal oscillation represented by Chikira–Sugiyama cumulus parameterization. Part II: Understanding moisture variation under weak temperature gradient balance. *J. Atmos. Sci.*, **71**, 615–639, https://doi.org/10.1175/JAS-D-13-038.1.

Fedorov, A. V., and W. K. Melville, 2000: Kelvin fronts on the equatorial thermocline. *J. Phys. Oceanogr.*, **30**, 1692–1705, https://doi.org/10.1175/1520-0485(2000)030<1692:KFOTET>2.0.CO;2.

——, and J. N. Brown, 2009: Equatorial waves. *Encyclopedia of Ocean Sciences*, 2nd ed. Elsevier, 271–287.

Gill, A. E., 1980: Some simple solutions for heat-induced tropical circulation. *Quart. J. Roy. Meteor. Soc.*, **106**, 447–462, https://doi.org/10.1002/qj.49710644905.

Haertel, P., 2018: Sensitivity of the Madden Julian oscillation to ocean warming in a Lagrangian atmospheric model. *Climate*, **6**, 45, https://doi.org/10.3390/cli6020045.

——, 2019: A Lagrangian ocean model for climate studies. *Climate*, **7**, 41, https://doi.org/10.3390/cli7030041.

——, 2021: Kelvin/Rossby wave partition of Madden–Julian oscillation circulations. *Climate*, **9**, 2, https://doi.org/10.3390/cli9010002.

——, and A. Fedorov, 2012: The ventilated ocean. *J. Phys. Oceanogr.*, **42**, 141–164, https://doi.org/10.1175/2011JPO4590.1.

——, G. N. Kiladis, A. Denno, and T. M. Rickenbach, 2008: Vertical-mode decompositions of 2-day waves and the Madden–Julian oscillation. *J. Atmos. Sci.*, **65**, 813–833, https://doi.org/10.1175/2007JAS2314.1.

——, K. Straub, and A. Fedorov, 2014: Lagrangian overturning and the Madden–Julian oscillation. *Quart. J. Roy. Meteor. Soc.*, **140**, 1344–1361, https://doi.org/10.1002/qj.2216.

——, W. Boos, and K. Straub, 2017: Origins of moist air in global Lagrangian simulations of the Madden–Julian oscillation. *Atmosphere*, **8**, 158, https://doi.org/10.3390/atmos8090158.

Heckley, W. A., and A. E. Gill, 1984: Some simple analytical solutions to the problem of forced equatorial long waves. *Quart. J. Roy. Meteor. Soc.*, **110**, 203–217, https://doi.org/10.1002/qj.49711046314.

Hendon, H. H., and B. Liebmann, 1990: The intraseasonal (30–50 day) oscillation of the Australian summer monsoon. *J. Atmos. Sci.*, **47**, 2909–2924, https://doi.org/10.1175/1520-0469(1990)047<2909:TIDOOT>2.0.CO;2.

Hoskins, B. J., and D. J. Karoly, 1981: The steady linear response of a spherical atmosphere to thermal and orographic forcing. *J. Atmos. Sci.*, **38**, 1179–1196, https://doi.org/10.1175/1520-0469(1981)038<1179:TSLROA>2.0.CO;2.

Hu, S., and A. V. Fedorov, 2019: Indian Ocean warming can strengthen the Atlantic meridional overturning circulation. *Nat. Climate Change*, **9**, 747–751, https://doi.org/10.1038/s41558-019-0566-x.

Hung, M.-P., J.-L. Lin, W. Wang, D. Kim, T. Shinoda, and S. J. Weaver, 2013: MJO and convectively coupled equatorial waves simulated by CMIP5 climate models. *J. Climate*, **26**, 6185–6214, https://doi.org/10.1175/JCLI-D-12-00541.1.

Janiga, M. A., J. Schreck III, J. A. Ridout, M. Flatau, N. P. Barton, E. J. Metzger, and C. A. Reynolds, 2018: Subseasonal forecasts of convectively coupled equatorial waves and the MJO: Activity and predictive skill. *Mon. Wea. Rev.*, **146**, 2337–2360, https://doi.org/10.1175/MWR-D-17-0261.1.

Jiang, X., 2017: Key processes for the eastward propagation of the Madden-Julian oscillation based on multimodel simulations. *J. Geophys. Res. Atmos.*, **122**, 755–770, https://doi.org/10.1002/2016JD025955.

——, and Coauthors, 2015: Vertical structure and physical processes of the Madden-Julian oscillation: Exploring key model physics in climate simulations. *J. Geophys. Res. Atmos.*, **120**, 4718–4748, https://doi.org/10.1002/2014JD022375.

Jin, F., and B. J. Hoskins, 1995: The direct response to tropical heating in a baroclinic atmosphere. *J. Atmos. Sci.*, **52**, 307–319, https://doi.org/10.1175/1520-0469(1995)052<0307:TDRTTH>2.0.CO;2.

Jones, C., D. E. Waliser, K. Lau, and W. Stern, 2004: Global occurrences of extreme precipitation and the Madden–Julian oscillation: Observations and predictability. *J. Climate*, **17**, 4575–4589, https://doi.org/10.1175/3238.1.

Kessler, W. S., and R. Kleeman, 2000: Rectification of the Madden–Julian oscillation into the ENSO cycle. *J. Climate*, **13**, 3560–3575, https://doi.org/10.1175/1520-0442(2000)013<3560:ROTMJO>2.0.CO;2.

Khairoutdinov, M., and K. A. Emanuel, 2019: Intraseasonal variability in near-global cloud-permitting simulations of an aquaplanet. *22nd Conf. on Atmospheric and Oceanic Fluid Dynamics*, Portland, ME, Amer. Meteor. Soc., 4, https://ams.confex.com/ams/22FLUID/meetingapp.cgi/Paper/359125.

Kiladis, G. N., K. H. Straub, and P. T. Haertel, 2005: Zonal and vertical structure of the Madden–Julian oscillation. *J. Atmos. Sci.*, **62**, 2790–2809, https://doi.org/10.1175/JAS3520.1.

——, M. C. Wheeler, P. T. Haertel, K. H. Straub, and P. E. Roundy, 2009: Convectively coupled equatorial waves. *Rev. Geophys.*, **47**, RG2003, https://doi.org/10.1029/2008RG000266.

Kim, D., A. H. Sobel, E. D. Maloney, D. M. Frierson, and I.-S. Kang, 2011: A systematic relationship between intraseasonal variability and mean state bias in AGCM simulations. *J. Climate*, **24**, 5506–5520, https://doi.org/10.1175/2011JCLI4177.1.

Kim, H., C. D. Hoyos, P. J. Webster, and I. Kang, 2008: Sensitivity of MJO simulation and predictability to sea surface temperature variability. *J. Climate*, **21**, 5304–5317, https://doi.org/10.1175/2008JCLI2078.1.

——, M. A. Janiga, and K. Pegion, 2019: MJO propagation processes and mean biases in the SubX and S2S reforecasts. *J. Geophys. Res. Atmos.*, **124**, 9314–9331, https://doi.org/10.1029/2019JD031139.

Lau, K.-M., and H. Lim, 1984: On the dynamics of equatorial forcing of climate teleconnections. *J. Atmos. Sci.*, **41**, 161–176, https://doi.org/10.1175/1520-0469(1984)041<0161:OTDOEF>2.0.CO;2.

——, and P. Chan, 1986: Aspects of the 40–50 day oscillation during the northern summer as inferred from outgoing longwave radiation. *Mon. Wea. Rev.*, **114**, 1354–1367, https://doi.org/10.1175/1520-0493(1986)114<1354:AOTDOD>2.0.CO;2.

Le Sommer, J., G. M. Reznik, and V. Zeitlin, 2004: Nonlinear geostrophic adjustment of long-wave disturbances in the shallow-water model on the equatorial beta-plane. *J. Fluid Mech.*, **515**, 135–170, https://doi.org/10.1017/S0022112004000229.

Liang, Y., and A. V. Fedorov, 2021: Linking the Madden-Julian oscillation, tropical cyclones and westerly wind bursts as part of El Niño development. *Climate Dyn.*, **57**, 1039–1060, https://doi.org/10.1007/s00382-021-05757-1.

——, ——, and P. Haertel, 2021: Intensification of westerly wind bursts caused by the coupling of the Madden-Julian oscillation to SST during El Niño onset and development. *Geophys. Res. Lett.*, **48**, e2020GL089395, https://doi.org/10.1029/2020GL089395.

Liebmann, B., H. H. Hendon, and J. D. Glick, 1994: The relationship between tropical cyclones of the western Pacific and Indian Oceans and the Madden-Julian oscillation. *J. Meteor. Soc. Japan*, **72**, 401–412, https://doi.org/10.2151/jmsj1965.72.3_401.

Lindzen, R. S., and S. Nigam, 1987: On the role of sea surface temperature gradients in forcing low-level winds and convergence in the tropics. *J. Atmos. Sci.*, **44**, 2418–2436, https://doi.org/10.1175/1520-0469(1987)044<2418:OTROSS>2.0.CO;2.

Madden, R. A., and P. R. Julian, 1972: Description of global-scale circulation cells in the tropics with a 40–50 day period. *J. Atmos. Sci.*, **29**, 1109–1123, https://doi.org/10.1175/1520-0469(1972)029<1109:DOGSCC>2.0.CO;2.

Majda, A. J., and S. N. Stechmann, 2009: The skeleton of tropical intraseasonal oscillations. *Proc. Natl. Acad. Sci. USA*, **106**, 8417–8422, https://doi.org/10.1073/pnas.0903367106.

——, and ——, 2011: Nonlinear dynamics and regional variations in the MJO skeleton. *J. Atmos. Sci.*, **68**, 3053–3071, https://doi.org/10.1175/JAS-D-11-053.1.

Maloney, E. D., 2009: The moist static energy budget of a composite tropical intraseasonal oscillation in a climate model. *J. Climate*, **22**, 711–729, https://doi.org/10.1175/2008JCLI2542.1.

——, and A. H. Sobel, 2007: Idealized hot spot experiments with a general circulation model. *J. Climate*, **20**, 908–925, https://doi.org/10.1175/JCLI4053.1.

Mapes, B., S. Tulich, J. Lin, and P. Zuidema, 2006: The mesoscale convection life cycle: Building block or prototype for large-scale tropical waves? *Dyn. Atmos. Oceans*, **42**, 3–29, https://doi.org/10.1016/j.dynatmoce.2006.03.003.

Matsuno, T., 1966: Quasi-geostrophic motions in the equatorial area. *J. Meteor. Soc. Japan*, **44**, 25–43, https://doi.org/10.2151/jmsj1965.44.1_25.

Matthews, A. J., 2008: Primary and successive events in the Madden–Julian oscillation. *Quart. J. Roy. Meteor. Soc.*, **134**, 439–453, https://doi.org/10.1002/qj.224.

McPhaden, M. J., 1999: Genesis and evolution of the 1997-98 El Niño. *Science*, **283**, 950–954, https://doi.org/10.1126/science.283.5404.950.

Monteiro, J. M., Á. F. Adames, J. M. Wallace, and J. S. Sukhatme, 2014: Interpreting the upper level structure of the Madden-Julian oscillation. *Geophys. Res. Lett.*, **41**, 9158–9165, https://doi.org/10.1002/2014GL062518.

Mori, M., and M. Watanabe, 2008: The growth and triggering mechanisms of the PNA: A MJO-PNA coherence. *J. Meteor. Soc. Japan*, **86**, 213–236, https://doi.org/10.2151/jmsj.86.213.

Moum, J. N., and Coauthors, 2014: Air–sea interactions from westerly wind bursts during the November 2011 MJO in the Indian Ocean. *Bull. Amer. Meteor. Soc.*, **95**, 1185–1199, https://doi.org/10.1175/BAMS-D-12-00225.1.

Nakajima, K., E. Toyoda, M. Ishiwatari, S.-I. Takehiro, and Y.-Y. Hayashi, 2004: Initial development of tropical precipitation patterns in response to a local warm SST area: An aqua-planet ensemble study. *J. Meteor. Soc. Japan*, **82**, 1483–1504, https://doi.org/10.2151/jmsj.82.1483.

Pegion, K., and B. P. Kirtman, 2008: The impact of air–sea interactions on the simulation of tropical intraseasonal variability. *J. Climate*, **21**, 6616–6635, https://doi.org/10.1175/2008JCLI2180.1.

Raymond, D. J., S. L. Sessions, A. H. Sobel, and Ž. Fuchs, 2009: The mechanics of gross moist stability. *J. Adv. Model. Earth Syst.*, **1** (3), https://doi.org/10.3894/JAMES.2009.1.9.

Rostami, M., and V. Zeitlin, 2020: Can geostrophic adjustment of baroclinic disturbances in the tropical atmosphere explain MJO events? *Quart. J. Roy. Meteor. Soc.*, **146**, 3998–4013, https://doi.org/10.1002/qj.3884.

Rui, H., and B. Wang, 1990: Development characteristics and dynamic structure of tropical intraseasonal convection anomalies. *J. Atmos. Sci.*, **47**, 357–379, https://doi.org/10.1175/1520-0469(1990)047<0357:DCADSO>2.0.CO;2.

Sentić, S., Ž. Fuchs-Stone, and D. J. Raymond, 2020: The Madden-Julian oscillation and mean easterly winds. *J. Geophys. Res. Atmos.*, **125**, e2019JD030869, https://doi.org/10.1029/2019JD030869.

Sherwood, S. C., T. Horinouchi, and H. A. Zeleznik, 2003: Convective impact on temperatures observed near the tropical tropopause. *J. Atmos. Sci.*, **60**, 1847–1856, https://doi.org/10.1175/1520-0469(2003)060<1847:CIOTON>2.0.CO;2.

Sobel, A., and E. Maloney, 2012: An idealized semi-empirical framework for modeling the Madden–Julian oscillation. *J. Atmos. Sci.*, **69**, 1691–1705, https://doi.org/10.1175/JAS-D-11-0118.1.

——, and ——, 2013: Moisture modes and the eastward propagation of the MJO. *J. Atmos. Sci.*, **70**, 187–192, https://doi.org/10.1175/JAS-D-12-0189.1.

——, S. Wang, and D. Kim, 2014: Moist static energy budget of the MJO during DYNAMO. *J. Atmos. Sci.*, **71**, 4276–4291, https://doi.org/10.1175/JAS-D-14-0052.1.

Sperber, K. R., 2003: Propagation and the vertical structure of the Madden–Julian oscillation. *Mon. Wea. Rev.*, **131**, 3018–3037, https://doi.org/10.1175/1520-0493(2003)131<3018:PATVSO>2.0.CO;2.

Stan, C., 2018: The role of SST variability in the simulation of the MJO. *Climate Dyn.*, **51**, 2943–2964, https://doi.org/10.1007/s00382-017-4058-2.

Wallace, J. M., and D. S. Gutzler, 1981: Teleconnections in the geopotential height field during the Northern Hemisphere winter. *Mon. Wea. Rev.*, **109**, 784–812, https://doi.org/10.1175/1520-0493(1981)109<0784:TITGHF>2.0.CO;2.

Wang, B., and H. Rui, 1990: Dynamics of the coupled moist Kelvin–Rossby wave on an equatorial β-plane. *J. Atmos. Sci.*, **47**, 397–413, https://doi.org/10.1175/1520-0469(1990)047<0397:DOTCMK>2.0.CO;2.

——, and X. Xie, 1997: A model for the boreal summer intraseasonal oscillation. *J. Atmos. Sci.*, **54**, 72–86, https://doi.org/10.1175/1520-0469(1997)054<0072:AMFTBS>2.0.CO;2.

——, and ——, 1998: Coupled modes of the warm pool climate system. Part I: The role of air–sea interaction in maintaining Madden–Julian oscillation. *J. Climate*, **11**, 2116–2135, https://doi.org/10.1175/1520-0442-11.8.2116.

Webster, P. J., 1981: Mechanisms determining the atmospheric response to sea surface temperature anomalies. *J. Atmos. Sci.*, **38**, 554–571, https://doi.org/10.1175/1520-0469(1981)038<0554:MDTART>2.0.CO;2.

Wheeler, M., and G. N. Kiladis, 1999: Convectively coupled equatorial waves: Analysis of clouds and temperature in the wavenumber–frequency domain. *J. Atmos. Sci.*, **56**, 374–399, https://doi.org/10.1175/1520-0469(1999)056<0374:CCEWAO>2.0.CO;2.

——, and H. H. Hendon, 2004: An all-season real-time multivariate MJO index: Development of an index for monitoring and prediction. *Mon. Wea. Rev.*, **132**, 1917–1932, https://doi.org/10.1175/1520-0493(2004)132<1917:AARMMI>2.0.CO;2.

Wolding, B. O., and E. D. Maloney, 2015: Objective diagnostics and the Madden–Julian oscillation. Part II: Application to moist static energy and moisture budgets. *J. Climate*, **28**, 7786–7808, https://doi.org/10.1175/JCLI-D-14-00689.1.

Yanai, M., S. Esbensen, and J.-H. Chu, 1973: Determination of bulk properties of tropical cloud clusters from large-scale heat and moisture budgets. *J. Atmos. Sci.*, **30**, 611–627, https://doi.org/10.1175/1520-0469(1973)030<0611:DOBPOT>2.0.CO;2.

Yoneyama, K., C. Zhang, and C. N. Long, 2013: Tracking pulses of the Madden–Julian oscillation. *Bull. Amer. Meteor. Soc.*, **94**, 1871–1891, https://doi.org/10.1175/BAMS-D-12-00157.1.

Zhang, C., 2005: Madden-Julian oscillation. *Rev. Geophys.*, **43**, RG2003, https://doi.org/10.1029/2004RG000158.

——, 2013: Madden–Julian oscillation: Bridging weather and climate. *Bull. Amer. Meteor. Soc.*, **94**, 1849–1870, https://doi.org/10.1175/BAMS-D-12-00026.1.

——, and J. Ling, 2017: Barrier effect of the Indo-Pacific Maritime Continent on the MJO: Perspectives from tracking MJO precipitation. *J. Climate*, **30**, 3439–3459, https://doi.org/10.1175/JCLI-D-16-0614.1.

——, Á. F. Adames, B. Khouider, B. Wang, and D. Yang, 2020: Four theories of the Madden-Julian oscillation. *Rev. Geophys.*, **58**, e2019RG000685, https://doi.org/10.1029/2019RG000685.